Atomically Resolved Anisotropic Electrochemical Shaping of Nano-electrocatalyst

Francisco Ruiz-Zepeda,[†,‡] Matija Gatalo,[†,§] Andraž Pavlišič,[∥] Goran Dražić,[†] Primož Jovanovič,[∥]
Marjan Bele,[†] Miran Gaberšček,[†,§] and Nejc Hodnik*[∥,⊥]

†Department of Materials Chemistry, National Institute of Chemistry, Hajdrihova 19, SI-1000 Ljubljana, Slovenia

‡Department of Physics and Chemistry of Materials, Institute of Metals and Technology, Lepi pot 11, SI-1000 Ljubljana, Slovenia

§Faculty of Chemistry and Chemical Technology, University of Ljubljana, Večna pot 113, SI-1000 Ljubljana, Slovenia

∥Department of Catalysis and Chemical Reaction Engineering, National Institute of Chemistry, Hajdrihova 19, SI-1000 Ljubljana,
Slovenia

⊥University of Nova Gorica, Vipavska 13, 5000 Nova Gorica, Slovenia

S *Supporting Information*

ABSTRACT: Catalytic properties of advanced functional materials are
determined by their surface and near-surface atomic structure,
composition, morphology, defects, compressive and tensile stresses, etc;
also known as a structure−activity relationship. The catalysts structural
properties are dynamically changing as they perform via complex
phenomenon dependent on the reaction conditions. In turn, not just the
structural features but even more importantly, catalytic characteristics of
nanoparticles get altered. Definitive conclusions about these phenomena
are not possible with imaging of random nanoparticles with unknown
atomic structure history. Using a contemporary PtCu-alloy electrocatalyst
as a model system, a unique approach allowing unprecedented insight into
the morphological dynamics on the atomic-scale caused by the process of
dealloying is presented. Observing the detailed structure and morphology
of the same nanoparticle at different stages of electrochemical treatment
reveals new insights into atomic-scale processes such as size, faceting, strain and porosity development. Furthermore, based on
precise atomically resolved microscopy data, Kinetic Monte Carlo (KMC) simulations provide further feedback into the
physical parameters governing electrochemically induced structural dynamics. This work introduces a unique approach toward
observation and understanding of nanoparticles dynamic changes on the atomic level and paves the way for an understanding of
the structure−stability relationship.

KEYWORDS: *Electrocatalysis, dealloying, fuel cells, identical location TEM, kinetic Monte Carlo*
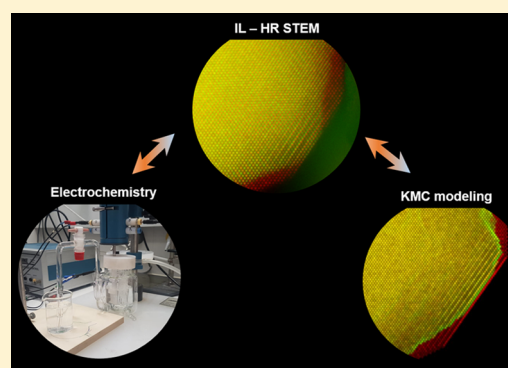
In the past decades, we have witnessed tremendous advances
in the core performance and understanding of the
structure−activity relationship of materials for potential use
in electrochemical devices such as fuel cells or electrolyzers.
Most of these materials, however, exhibit dynamic changes in
morphology, structure, and composition, especially when
exposed to the harsh electrochemical environment found in
the aforementioned applications. In the case of low-temper-
ature proton exchange membrane fuel cells (PEMFC), one of
the most studied systems are platinum alloys, which represent
the state-of-the-art cathode electrocatalysts.[1] It is well-known
that structural properties on the atomic level of the Pt surface
and near-surface regions[2,3] such as morphology,[4] composi-
tion,[5] nature of exposed facets,[6] presence of defects,[7,8] and
compressive and tensile stresses[9,10] govern the electrocatalytic
activity of Pt-based nanoalloy materials. Thus, it is very
important to understand and in the future also control the

atomic-scale structural dynamics of these nanoparticles in
order to achieve optimal stability.

In an effort to better understand the structure−stability
relationship and its related mechanisms, new methods and
techniques have been proposed and developed in electron
microscopy,[11] synchrotron spectroscopy,[12−14] and different
analytic tools such as the online coupling of electrochemical
cells to ICP-MS.[15−17] As in regard to electron microscopy, an
ideal setup would involve an in situ technique employing an
appropriate electrochemical liquid cell, which could allow the
observation of the solid active material at the atomic level with
minimal influence of the beam with the specimen, well-known
reactions and liquid electrolyte. Whereas a variant of such
direct methods for observation of electrochemically induced

structural dynamics of materials has been successfully demonstrated, this approach is still limited in resolution mainly by radiation damage.[18,19] In a nonelectrochemical variant of in situ liquid transmission electron microscopy (TEM) study that was performed without electrochemical control (without electrodes), Wu et al.[20] investigated the dissolution kinetics of oxidative etching in cubic and icosahedral Pt nanoparticles. The authors found that on icosahedron particles the corners had the highest dissolution rates, followed by the edges (with 2 orders of magnitude lower rates) and with the dissolution of terraces being the slowest. Among the flat surfaces (terraces) the hierarchy of facet selectivity was found to be the following: {110} cube > {100} cube > {111} icosahedron. However, the authors also noticed that the etching rate of Pt{111} facets was close to the etching rate of Pt{100} facets, suggesting that Pt{111} facets experience tensile strain that would facilitate atom removal. Another recent work by Dai et al.[21] reported facet-dependent oxidation of Pt_3Co nanoparticles under an in situ gas TEM (without liquid) experiment. Specifically, the authors show that Co segregation and oxidation take place preferentially on {111} surface facets but not on {100} surface facets, implying that {100} surface facets may maintain the activity of disordered Pt_3Co oxygen reduction reaction (ORR) catalyst.

Ex situ microscopy studies on the degradation of Pt-based nanoalloy materials have been widely used in the field of electrocatalysis.[22−25] Although, there is at least one potential limitation of state-of-the-art ex situ microscopy approach that needs to be considered. It is related to a statistical uncertainty about whether or not the nanoparticles size, morphology, structure, composition, and so forth, observed after electrochemical treatment on a limited number of surface spots can be considered representative for the whole material. Apart from the electrochemical environment to which the electrocatalyst is exposed, the parameters influencing nanoparticles' change are their initial size, chemical composition, morphology, as well as proximity to other neighboring nanoparticles. Furthermore, the nature, structure, and morphology of the supporting material is important as well. Because nanoparticles' history is not known in the random ex situ imaging, clear and accurate conclusions cannot be made for each nanoparticle, especially when going to atomic resolution. Thus, only general statistical descriptive insights are possible while the interpretation of before and after is usually also prone to the observational bias of the operator. This issue presents a big uncertainty and big dilemma, which can, however, be elegantly eliminated using the identical location electron microscopy (IL-EM) approach.[26−29] This approach is based on a quasi in situ repetitive process consisting of observation under a microscope, electrochemical treatment in an electrochemical cell, rinsing/drying followed by a second observation. As the name suggests, this technique allows the examination of the same spot throughout different stages of, for example, a degradation/stability protocol. Although one IL-EM spot does not provide the statistical description of the entire sample, it does allow for the possibility to track the exact history of the observed area and thus extract direct information on the different phenomena occurring at different stages that are a genuine consequence of electrochemical treatment or reaction conditions. This is shown on a preceding work about the stability of spherical $PtCu_3$ nanoparticles supported on a high surface area carbon,[30] where the authors observed by IL-EM that porosity formation and reshaping of $PtCu_3$ nanoparticles

depended on whether potentiostatic (potential hold) conditions or potentiodynamic (potential cycling) conditions were used.

With recent improvements in imaging resolution, in particular by using the possibilities offered by aberration-corrected scanning TEM (AC-STEM), it is possible to perform observations of electrochemically treated materials at the atomic scale. Whereas current high-resolution transmission electron microscopes regularly provide atomic resolution for various cases of interest, studies reporting an atomic resolution insight into degradation on identical location are still very scarce.[16,31,32] Atomic resolution imaging combined with the known history of the material on IL provide very accurate information about the evolution of the structure during stability testing. Because each nanoparticle is slightly different, observing several different nanoparticles should allow all the necessary statistics to describe the correlation between the sample's overall activity and stability and its structural development. In an ideal case, such fundamental atomistic understanding of the operation and degradation mechanisms on the given sample can help predict general trends in the broader family of such materials (alloyed catalyst, nanoshaped catalyst, non-PGM catalyst, and so forth). This can be considered a bottom-up approach to the overall understanding of how advanced functional materials change as they perform.

The degradation of Pt-based alloy nanoparticles will depend on the content and local distribution of the elements present; a third element may effectively improve the stability of such binary Pt-based catalyst.[33,34] In our previous study, introducing a third element not only reduced pore formation after EA but additionally, as shown experimentally and explained by kinetic Monte Carlo (KMC) simulations, changed the evolution of nanoparticle shape due to modified properties of Pt-skin.[35] These preliminary studies demonstrated a high complexity and interdependence of the processes occurring during EA. In any case, new and more systematic approaches have to be undertaken that can resolve these processes at the atomic scale.

In this work, we demonstrate the capacity of the atomic-scale IL-STEM by studying the electrochemical dealloying of a $PtCu_3$ nanoalloy electrocatalyst model system. This particular system was selected because a large amount of microstructural information is already available and can serve as quality reference data.[34−36] The $PtCu_3$ nanoparticles have a microstructure with an order−disorder interface and a Pt skin cover.[36] In the as-prepared state, their surface composition may not be homogeneous.[34,35] In addition, the material has shown a high electrical and thermal conductivity,[37] as well as stability under the electron beam,[38] partially due to its relatively larger size, in contrast to beam-sensitive and limited size nanoparticles.[39,40] We note that the formation of high energy surface atoms might not be accessible by the electron microscopy. For this experiment, we have advisedly chosen to perform a milder EA (0.1 M $HClO_4$, 0.05−1.2 V_{RHE}, 300 mV $s^{−1}$, 200 cycles) in order to observe early pore formation and reshaping, which is experimentally relatively unexplored.[41] The choice of the phenomenon of dealloying is justified by the fact that binary alloys of platinum with transition metals are known to undergo distinct compositional, structural and morphological transformation after being subjected to electrochemical acidic treatment; this complexity makes them very much suitable for the present purposes, that is, identification of governing mechanisms leading to transformation/degradation of as prepared material.
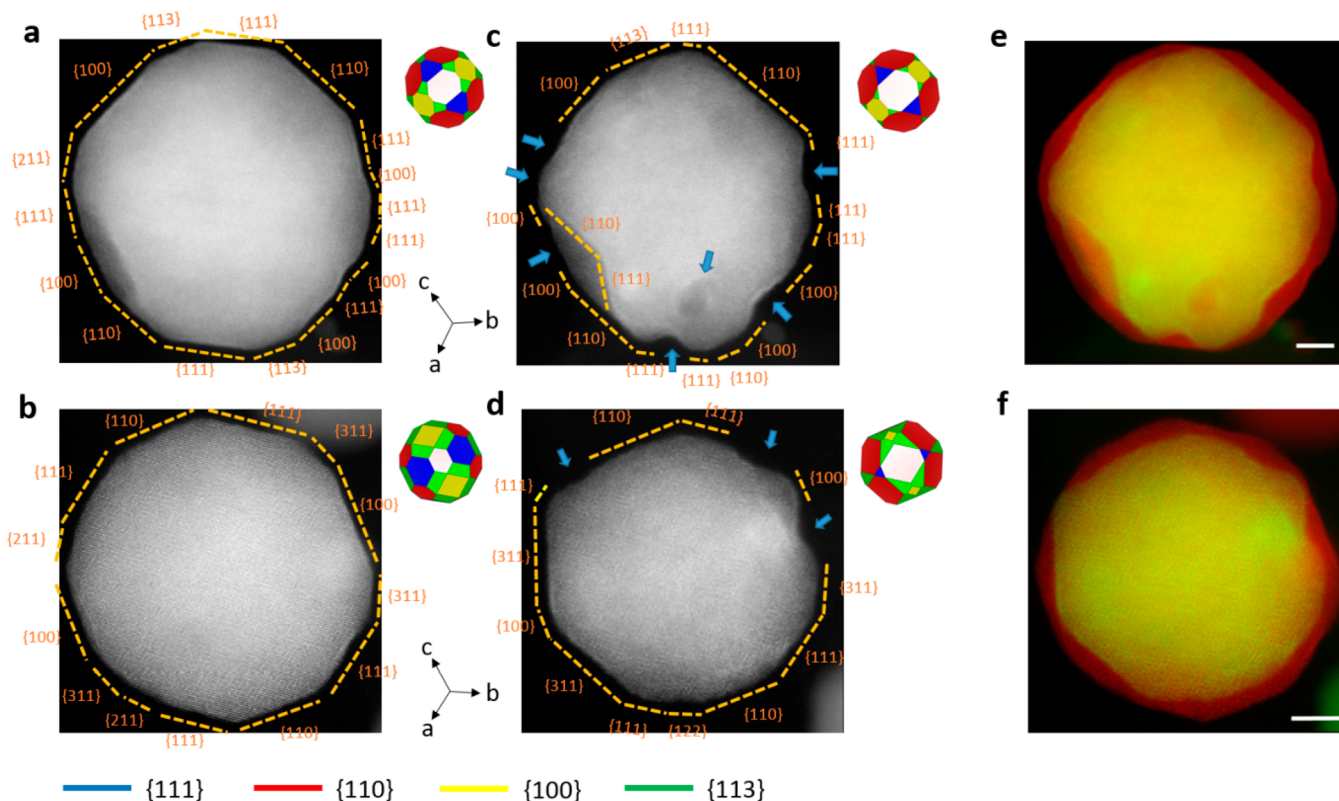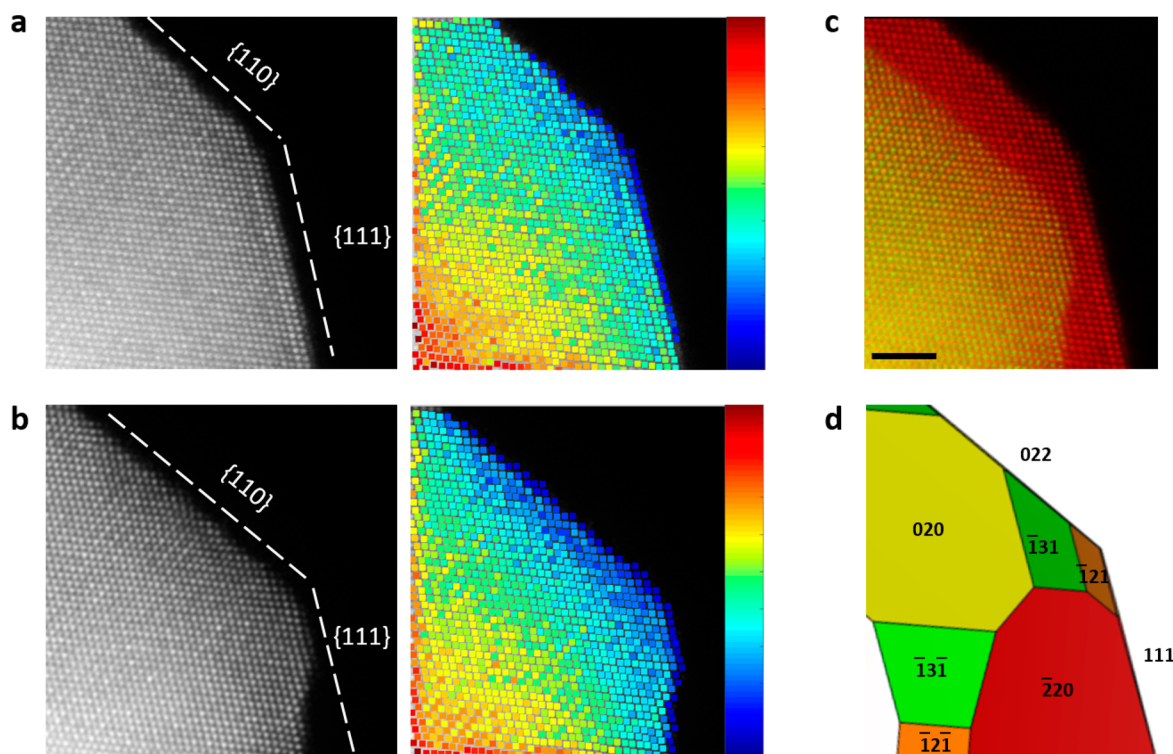
Figure 1. Identical-location AC-STEM ADF images of [110] oriented $PtCu_3$ nanoparticles before and after mild electrochemical activation. As-prepared state (before electrochemical activation) of (a) a twinned nanoparticle and (b) a defect-free nanoparticle. Surface facets planes are identified and marked accordingly. (c,d) Respective nanoparticles after EA showing surface etching and pore formation. Dents due to surface etching are indicated with arrows. An ideal geometric model with symmetric facets is portrayed in the right upper corner of each nanoparticle image. The facet color code is shown at the bottom. (e,f) Overlay images of both states of the nanoparticles, before EA (red), and after EA (green). Scale bar is 5 nm.

To track the morphological changes occurring at the same catalyst nanolocation during progressive electrochemical treatment, we deposited as-prepared $PtCu_3/C$ nanoparticles[36] on a gold finder TEM grid. Several spots were identified on the TEM grid and imaged at different magnifications (Figure S1 and Figure S2). The regions of interest (ROI) selected for the identical location imaging were kept under a reduced electron dose in order to avoid or minimize any induced modification with the beam[42] (see the experimental section in Supporting Information and Figure S3 for further details). Severe electron exposure, such as beam alignment and elemental mapping with energy dispersive X-ray spectroscopy (EDX) were not performed on the selected spots. Care was taken on the irradiation time and beam intensity despite the relatively large size (20−30 nm) of the chosen $PtCu_3$ nanoparticles, which can help reduce the effect of the electron beam, since the surface of nanocrystals can be easily damaged compared to the bulk.[43] After performing the EA IL-TEM protocol,[26] some of the STEM annular dark-field (ADF) experimental images were denoised using a nonlinear filter.[44]

Four important properties of nanoparticles are studied at selected identical locations for the first time. First, the effect of particle size reduction (shrinking) due to dealloying is measured. Second, anisotropic facet development is tracked at the atomic-scale with facet identification. Third, early pore formation is imaged and discussed. Finally, the strain at different surface facets is estimated from the registered atomic positions in the images. In addition, our observations are

supported by atomically resolved KMC simulations performed on a single $PtCu_3$ nanoparticle for the interpretation of all four phenomena.

Figure 1 shows the structure and morphology of $PtCu_3$ nanoparticles before and after electrochemical activation. The morphology of two different nanoparticles (sequences a-c-e and b-d-f in Figure 1) with different surface geometries and microstructures (a twinned and a defect-free nanoparticle, Figure S4) is observed before (Figure 1a,b) and after (Figure 1c,d) a typical electrochemical activation treatment of alloyed electrocatalysts (0.1 M $HClO_4$, 0.05−1.2 V_{RHE}, 300 mV s^{-1}, 200 cycles[17,36]). For easier comparison, an overlay of the images taken before and after EA is depicted in Figures 1e,f for each particle. The overlay shows a reduction of the nanoparticles size after EA due to the removal of Cu. The so-called dealloying process leaves behind a nanostructured surface, also referred to as skeleton type surface[7] or even pores.[35,45,46] To estimate how much of the volume of the nanoparticle is reduced, the area within the contour of the image of the nanoparticle is calculated and the volume extrapolated (Figure S5). After EA, the nanoparticle volume was reduced by about 16−26%. This particular finding is important because the shrinking of nanoparticles after dealloying is commonly overlooked. Thus, the physical picture or even the model is usually oversimplified, quite commonly exhibiting the formation of a Pt shell, however without any decrease in particle size after dealloying.[46]
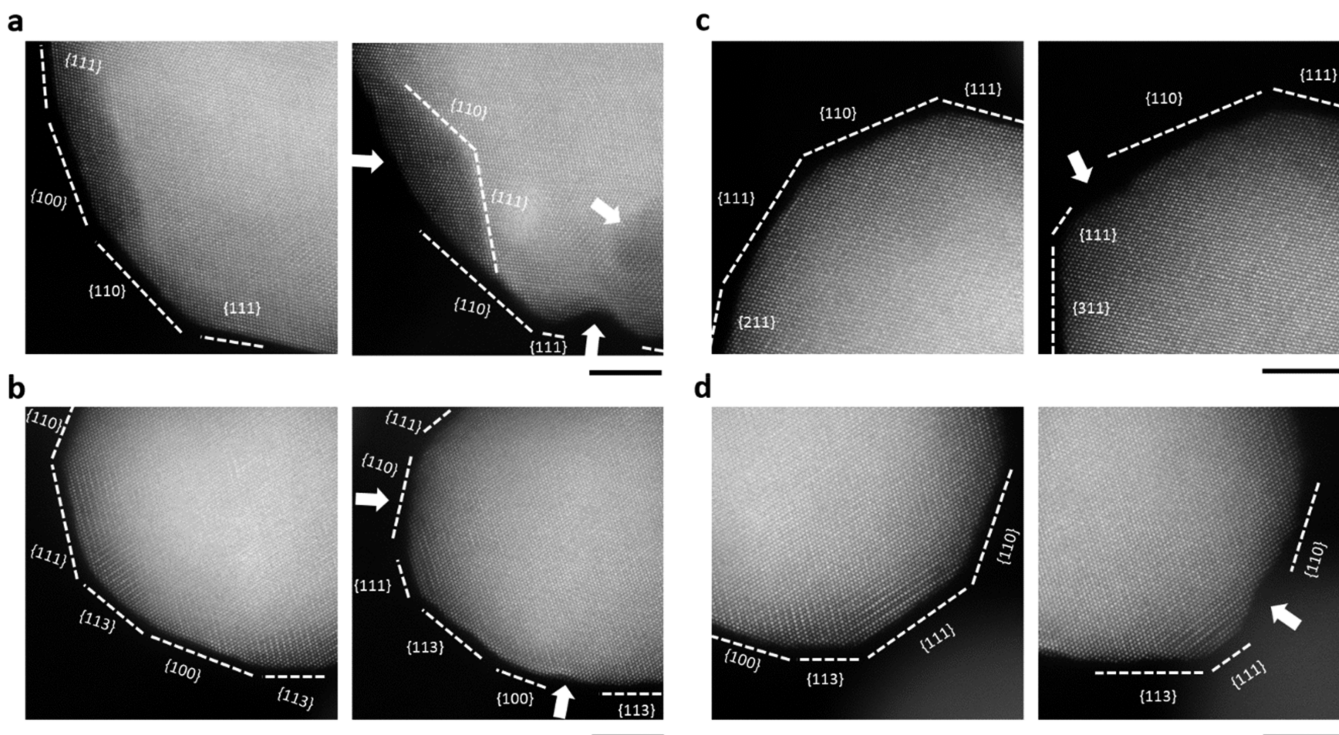
Figure 2. Identical-location AC-STEM ADF images of one section of a nanoparticle (a) before EA and (b) after EA, and their corresponding relative image intensity of the atomic columns. (c) Overlay of the two ADF images from before EA (red) and after EA (green). (d) The 3D geometric facet model. Scale bar is 2 nm.

In addition to etching and pore formation, the present approach also precisely follows other important phenomena such as particle reshaping (compare Figure 1a,c and b,d). Reshaping of Pt-alloy nanoparticles after EA was already observed before, however, the exact mechanism has not yet been explained in detail.[25,30,36] By following the evolution of faceting with high-resolution IL-STEM it is possible to provide an analysis of such phenomena and further elaborate on the unanswered queries. In Figure 1c, the twinned nanoparticle exhibits a uniform etching along the {110} facets but a nonuniform etching along the {100} and {111} facets. The defect-free nanoparticle displayed in Figure 1d shows a similar type of behavior after dealloying, however with a more pronounced reshaping. Here we should mention that the initial shape of both nanoparticles is not the same, this information is quite important since the final facet configuration after EA would depend on the initial geometrical shape of the nanoparticle. An ideal three-dimensional (3D) geometrical model (constructed assuming a symmetric configuration, although the 3D structure can be more complex[47]) is depicted in the right upper corner of each nanoparticle image in Figure 1. From the 3D geometric model, it is also possible to visualize that facets such as {110} increase in size whereas facets corresponding to {111} are reducing in size after EA. It is very intriguing to see how the {111} facet is disappearing although it is considered as the most stable due to the highest coordination number of the surface atoms. However, if we consider that the less stable facet is actually the one which is dissolving, then it becomes rather clear why the {110} facet is getting larger and the {111} facet is disappearing. This observation on the facet development dynamics provided us with a first general approach in the interpretation of the complex phenomena of particle faceting. Since no two particles

are completely identical, especially in the real-industry relevant samples, the presence of different facets with different initial sizes plays a decisive role in the formation of the exact final geometrical shape of the nanoparticle. Additionally, besides the factors such as size, structure, interaction with the support, etc., the parameter that strongly affects the final shape of nanoalloys is the initial chemical composition of the nanoparticles' surface facets, which further complicates the evolution of such materials. In the same context, we note that in alloys the (re)shaping is thus not just a reconstruction process since atoms are not only moved to new places on the nanoparticle but some of them (mostly copper) are completely removed (dealloyed) from the nanoparticle.

To further explore and elucidate the phenomenon of faceting, a selected section of the nanoparticle displayed in Figure 1a,c is shown in Figure 2a,b. The images are accompanied by the corresponding intensity map of the individual atomic columns, obtained by a quantification algorithm developed by De Backer et al.[48] The intensity of each atomic column imaged by high-angle ADF (HAADF) is sensitive to the atomic Z-number, but also has a dependence on the mass thickness.[49,50] In Figure 2 atomically resolved IL-STEM ADF shows the facet structure and morphology evolution before and after EA. Specifically, in Figure 2a the imaged section of the as-prepared $PtCu_3$ nanoparticle corresponds to the meeting edge of surface facets {110} and {111}. After electrochemical activation, the corner is truncated (Figure 2b), and a dent along the {111} facet forms due to nonuniform (anisotropic) etching, turning it into a rough surface. Simultaneously, etching along the {110} direction is observed in a uniform manner, hence increasing the size of the {110} facet (Figure 2c). A more revealing feature can be visualized on the corresponding intensity image of individual

Figure 3. Identical location AC-STEM ADF images of sections of nanoparticles. Left is before EA and right is after EA in all images. (a) Pores and dents originating due to etching. (b) Etching of {110} facet and size reduction of {111} facet. Additionally, a small dent is occurring at {100} facet, marked with an arrow on the bottom. (c) Surface reshaping due to etching of {110} facet. Size reduction of {111} facet and the formation of a stepped surface due to nonuniform etching. (d) Size reduction of {111} facet and nonuniform etching indicated by the arrow on the side. Scale bar is 5 nm.
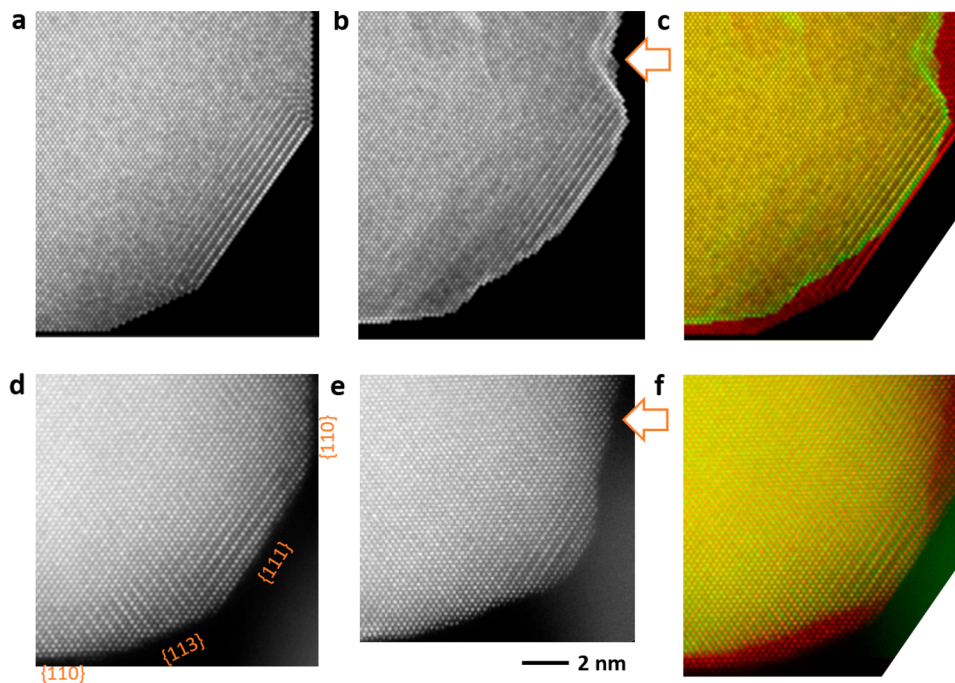
Figure 4. (a−c) KMC simulation of PtCu₃ nanoparticle. (a) Initial condition in the KMC model. (b) After dealloying in the KMC model. White arrow marks a dent on {110} facet. (c) Overlay of the two models. (d−f) AC-STEM ADF images of a PtCu₃ nanoparticle. (d) Initial condition before EA. (e) Dealloying condition after EA. (f) Overlay of the two images. The exposed area of the {111} facet is reduced after EA, leaving a nonuniform stepped surface.

atomic columns in Figure 2b; in this image, the section of the nanoparticle has now an evident wedge-like shape along the {110} facet when compared to the intensity image from Figure

2a. This can be considered as an indication that etching has also occurred at the top and bottom from our field of view of the nanoparticle, meaning that the section was not only
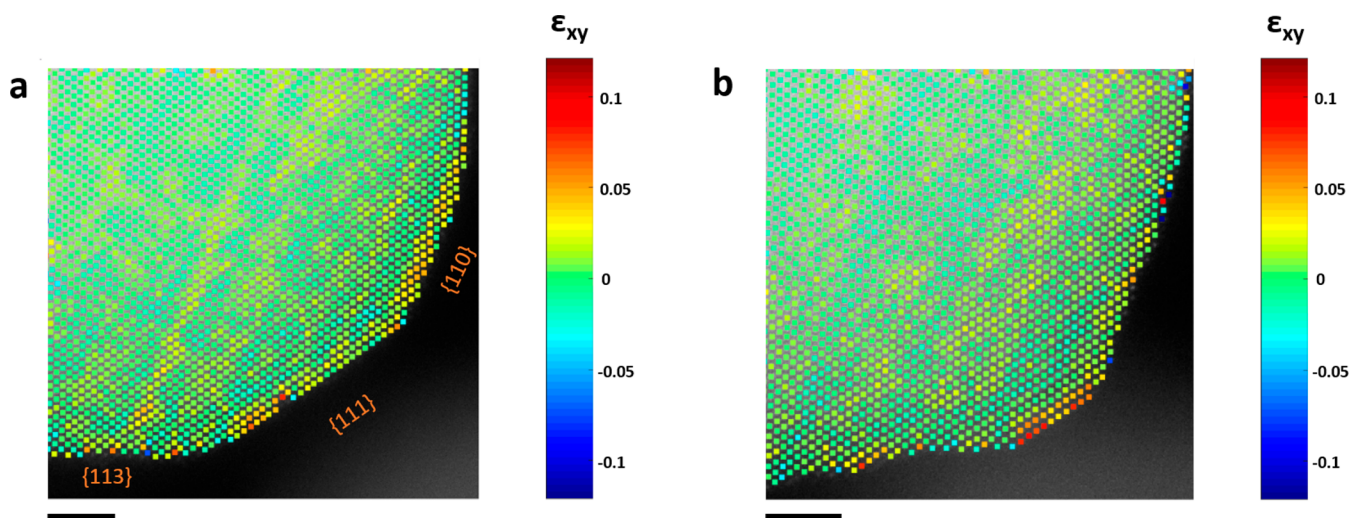
Figure 5. Strain analysis in a section of a PtCu$_3$ nanoparticle. (a) Shear strain ε_{xy} map before EA and (b) after EA. Scale bar is 2 nm.

modified from the visible surfaces but also has a thinner thickness since the obtained STEM ADF images are a 2D projection of 3D matter. This observation raises the question of which additional neighboring facets are being etched beside the observed {110} facet. By gathering data from the surface facets of the nanoparticles in Figures 1a,b and assuming a symmetrical shape, a 3D geometrical model is constructed illustrating the surface facet planes of this specific section of the nanoparticle, as shown in Figure 2d. The perspective of the 3D geometric model unveils surface facets planes {131} and {121} as the unstable facets, along with the {110} facets. Because of the complexity of the dealloying process and despite several factors affecting the evolution of the surface and shape of the nanoparticle during an electrochemical process, we observed a common trend during our experiments that allowed us to use KMC simulations and compare them to the observations. This is detailed in the following paragraphs.

The crucial role of faceting is further illustrated by studying the pore formation in more detail, as shown in Figure 3, where a close up on sections of nanoparticles illustrates pores, etching and reshaping. The initial stage of pore formation is denoted with arrows in Figure 3a. After EA a dent has formed at the bottom of the nanoparticle on the {111} facet by a nonuniform etching. Additionally, a pore has appeared very close to the dent and can be distinguished by the spot with a darker contrast in the nanoparticle. A slight etching of the {100} surface facet is manifested by the creation of a defected stepped surface (also referred to as skeleton type surface[51]) and is accompanied by the formation of neighboring facets {110} and {111}. In Figure 3b, the size of the {111} facet is reduced by side etching of the {110} facet and the formation of a stepped surface. Additionally, a small dent has started to form at the bottom of the nanoparticle at the {100} facet. In Figure 3c the size of {111} facet has been reduced, whereas the size of the neighboring facet {110} has increased, however, with the formation of a stepped surface. Moreover, there is a substitution of a {211} facet for a {311} facet next to the {111} facet of the nanoparticle. Similarly, in Figure 3d the size of {111} facet has been reduced due to a nonuniform side etching of the neighboring facets {110} and {113}. This event takes place together with the creation of a stepped surface. In all these four cases, the size of {111} facet has decreased while that of the {110} facet has increased, suggesting that facet

dissolution occurs anisotropically in the following order {110} > {100} > {111}. In addition to this process, early pore formation was observed. We believe that pores start to form at the copper-rich regions.

Using the information obtained from the previously recorded atomic structure of the pristine nanoparticle as an initial condition, the dealloying of PtCu$_3$ nanoparticles was simulated by the KMC method (further information on the simulation progression can be found in the Supporting Information), as shown in Figure 4a−c. It is worth mentioning that depending on whether the result of KMC simulation matches the real IL-TEM experiment, the feedback information is obtained on whether the current understanding or physical model is feasible. Previous studies have shown that structural intermetallic order in PtCu$_3$ nanoparticles slows down the dealloying effect[52] and leads to a less porous configuration and a smoother surface (Figure S6). According to our physical model, the two key factors governing the delloying process are dissolution and surface diffusion. In our case, Cu is the dissolving metal and Pt is moving freely on the surface. Both phenomena are dependent on the coordination numbers of the surrounding atoms. Depending on the ratio between the rates or frequencies of these two processes the PtCu$_3$ nanoparticle can develop porosity or completely defectless structure. The best fit to our experiments was obtained by a moderate dissolution/diffusion ratio (Figure S7). This result gives a broader view of which possibilities could enable a better description of the different observed conditions in the experimental part, importantly, within the same nanoparticle. As observed in Figure 4a−c, the process of dealloying is transforming the {111} facet, leaving behind a nonuniform etched and stepped surface. This phenomenon is also observed experimentally on the PtCu$_3$ nanoparticles, as exemplified in Figure 4d−f where a section of a nanoparticle is imaged before and after EA. The surface is etched nonuniformly, reducing the size of the {111} facet and creating a stepped surface, potentially also an early stage of pore formation. Other cases in which facets become uniformly etched are described in Figure S7. An interesting outcome of the KMC simulations was that chemical inhomogeneity on the surface of the nanoparticle, that is, having an imperfect Pt skin, different chemical order, or a higher local concentration of copper significantly affects the dealloying process at the facets

like, for instance, the influence of the initial Pt-skin layer thickness and porosity formation.[35] Interestingly, IL-TEM observations could not be reproduced if Pt-skin and local chemical compositions were not altered. A 3D visual composition of the simulated nanoparticles is illustrated in Movies 1, 2, 3, 4, and 5 from Supporting Information along with 3D visual animated images describing initial and dealloying conditions of the nanoparticles. Surface dents or cavities similar to the ones identified previously on nanoparticles as in {110} facets are also distinguishable on the KMC simulated dealloyed Movies 3 and 5, as the one marked in Figure 4b. Three-dimensional visualization and animations are very useful to better perceive the studied event. Our KMC results closely describe several phenomena occurring on PtCu$_3$ nanoparticles and at the same time provide evidence on the validity of the model.

Surface strain is another very important parameter governing the ORR activity and stability of the Pt-alloys via size mismatch of less noble metal atoms below the catalytically active Pt surface atoms.[53] As strain can facilitate the dealloying and increase or reduce the catalytic reaction depending on which facet is acting,[9] it is of great interest to track how the strain unfolds across the facets due to the electrochemical restructuring. This is illustrated in Figure 5, where the images taken before and after EA of one section of a nanoparticle are analyzed in terms of strain, by using the information obtained from the extracted atomic column positions, and calculating derivatives from the measured displacements of the atomic columns when compared to an ideal reference (similar to the approach used in peak pairs analysis).[54−56] We notice that initially the strain distribution is on {110}, partially on {111}, and with some variations on {113}. However, after EA the strain is accumulated on {111} due to a strong influence from the edges and distributed on the steps and kinks formed at the surfaces {110} and {113} (also visible on additional strain maps included in Figure S8). Surface strain will depend on the number of Pt monolayers on the surface however edge and corner sites are expected to experience larger strain than surface facet sites.[57] In the end, it will be a contribution and an interplay between the particle size, misfit strain, skin thickness and intrinsic surface strain.[58] Inherently, the lower coordination number of surface atoms (compared to bulk atoms) will induce some internal strain in order to reduce the surface energy,[59] placing {111} with the lowest strain after {100} and {110} (coordination numbers 9, 8, 7, respectively; Figure S9). From our analysis, the {100} planes are the richest in Pt (Figure S10), followed very closely by {111} planes and last by {110} planes, which exhibits the lowest amount of Pt, and hence tends to experience less strain. The IL-STEM images reveal that etching occurs preferentially in the following order: {110} > {100} > {111}. However, {111} facets are Pt-rich; in terms of bonding, when comparing surface atoms of different facets, it would be more difficult to remove an atom with higher coordination number than an atom with lower coordination number. Hence, we would expect a higher resistance toward dealloying in the following order: {111} > {100} > {110}. The {111} facets are the least favorable surface sites for Cu segregation,[60] resulting in {111} Pt-rich surfaces, since they have the lowest surface energy among the three low index planes in face-centered cubit (fcc) metals: $\gamma_{111} < \gamma_{100} < \gamma_{110}$.[61−63] However, this hierarchy in the energy sequence may be modified if the structure corresponds to an ordered alloy in the PtCu system as the surface energy inequality between the

{100} and {111} facets can reverse to $\gamma_{100} < \gamma_{111}$.[64] This effect may explain the striving of Pt atoms to segregate to {100} and {111} facets. On the other hand, in high Cu content, Cu atoms will most favorably occupy sites with lower coordination number:[60] the vertex, next the edge, and later the {100} and {111} facet sites, conversely to Pt.

In summary, by using atomic-resolution IL-STEM and examining PtCu$_3$ nanoparticles before and after electrochemical potential cycling activation, we have revealed several important dynamic phenomena, such as particle size reduction, the occurrence of pore formation, facet etching selectivity, straining, as well as anisotropic facet dissolution that proceeds in the following order {110} > {100} > {111}. Kinetic Monte Carlo simulations indicated that apart from the dissolution/diffusion ratio, a slight alteration in the near-surface composition influences the formation of porosity as well as the facet etching mechanism. Since the dissolution/diffusion ratio can be regarded as an imitation of the electrochemical treatment potential, we expect that nanoparticles built only with {111} facets (octahedron polyhedron) would have a better chance to resist the degradation phenomena caused by ORR than any other shape. However, it is important to state that this will only be effective if the corners and edges of the facets are stabilized, for instance with Rh, Au, Ir.[34,65,66] Our findings of selective facet dissolution could open the door to a better understanding of stability and thus prolonged performance via atomistic surface design of alloy nanoparticles.

■ ASSOCIATED CONTENT

Ⓢ Supporting Information

The Supporting Information is available free of charge on the ACS Publications website at DOI: 10.1021/acs.nanolett.9b00918.

> Experimental section, Figure S1 explaining IL-TEM approach, Figure S2 showing IL-(S)TEM, Figure S3 showing two STEM ADF images of PtCu$_3$ nanoparticle from Figure 1a, Figure S4 showing STEM micrographs of PtCu$_3$ nanoperticles with and without twins, Figure S5 showing STEM micrographs and shrinking of PtCu$_3$ nanoparticles, further information on the KMC simulation progression, Figure S6 and S7 showing KMC results, Figure S8 showing strain maps, Figure S9 showing models of different unreconstructed surface facet planes, Figure S10 showing processed images of particles from Figure 1 (PDF)
> Three dimensional kinetic Monte Carlo simulation of PtCu3 nanoparticles showing particle density (AVI)
> Three dimensional kinetic Monte Carlo simulation of PtCu3 nanoparticles showing initial condition (AVI)
> Three dimensional kinetic Monte Carlo simulation of PtCu3 nanoparticles after dealloying (AVI)
> Three dimensional kinetic Monte Carlo simulation of PtCu3 nanoparticles showing initial condition (rendering) (AVI)
> Three dimensional kinetic Monte Carlo simulation of PtCu3 nanoparticles after dealloying (rendering) (AVI)

■ AUTHOR INFORMATION

Corresponding Author

*E-mail: nejc.hodnik@ki.si.

ORCID Ⓞ

Francisco Ruiz-Zepeda: 0000-0002-2637-3433

Matija Gatalo: 0000-0002-5041-7280
Primož Jovanovič: 0000-0003-2477-3895
Miran Gaberšček: 0000-0002-8104-1693
Nejc Hodnik: 0000-0002-7113-9769

Author Contributions

The manuscript was written through contributions of all authors. All authors have given approval to the final version of the manuscript.

Notes

The authors declare no competing financial interest.

■ REFERENCES

(1) Seh, Z. W.; Kibsgaard, J.; Dickens, C. F.; Chorkendorff, I.; Nørskov, J. K.; Jaramillo, T. F. *Science* **2017**, *355*, eaad4998.

(2) Stephens, I. E. L.; Bondarenko, A. S.; Perez-Alonso, F. J.; Calle-Vallejo, F.; Bech, L.; Johansson, T. P.; Jepsen, A. K.; Frydendal, R.; Knudsen, B. P.; Rossmeisl, J.; Chorkendorff, I. *J. Am. Chem. Soc.* **2011**, *133*, 5485−5491.

(3) Escudero-Escribano, M.; Malacrida, P.; Hansen, M. H.; Vej-Hansen, U. G.; Velázquez-Palenzuela, A.; Tripkovic, V.; Schiøtz, J.; Rossmeisl, J.; Stephens, I. E. L.; Chorkendorff, I. *Science* **2016**, *352*, 73−76.

(4) Chen, C.; Kang, Y.; Huo, Z.; Zhu, Z.; Huang, W.; Xin, H. L.; Snyder, J. D.; Li, D.; Herron, J. A.; Mavrikakis, M.; Chi, M.; More, K. L.; Li, Y.; Markovic, N. M.; Somorjai, G. A.; Yang, P.; Stamenkovic, V. R. *Science* **2014**, *343*, 1339−1343.

(5) Greeley, J.; Stephens, I. E. L.; Bondarenko, A. S.; Johansson, T. P.; Hansen, H. A.; Jaramillo, T. F.; Rossmeisl, J.; Chorkendorff, I.; Nørskov, J. K. *Nat. Chem.* **2009**, *1*, 552−556.

(6) Stamenkovic, V. R.; Fowler, B.; Mun, B. S.; Wang, G.; Ross, P. N.; Lucas, C. A.; Marković, N. M. *Science* **2007**, *315*, 493−497.

(7) Stamenkovic, V. R.; Mun, B. S.; Arenz, M.; Mayrhofer, K. J. J.; Lucas, C. A.; Wang, G.; Ross, P. N.; Markovic, N. M. *Nat. Mater.* **2007**, *6*, 241−247.

(8) Calle-Vallejo, F.; Tymoczko, J.; Colic, V.; Vu, Q. H.; Pohl, M. D.; Morgenstern, K.; Loffreda, D.; Sautet, P.; Schuhmann, W.; Bandarenka, A. S. *Science* **2015**, *350*, 185−189.

(9) Strasser, P.; Koh, S.; Anniyev, T.; Greeley, J.; More, K.; Yu, C.; Liu, Z.; Kaya, S.; Nordlund, D.; Ogasawara, H.; Toney, M. F.; Nilsson, A. *Nat. Chem.* **2010**, *2*, 454−460.

(10) Chattot, R.; Le Bacq, O.; Beermann, V.; Kühl, S.; Herranz, J.; Henning, S.; Kühn, L.; Asset, T.; Guétaz, L.; Renou, G.; Drnec, J.; Bordet, P.; Pasturel, A.; Eychmüller, A.; Schmidt, T. J.; Strasser, P.; Dubau, L.; Maillard, F. *Nat. Mater.* **2018**, *17*, 827−833.

(11) Su, D. S.; Zhang, B.; Schlögl, R. *Chem. Rev.* **2015**, *115*, 2818−2882.

(12) Mukerjee, S.; Srinivasan, S.; Soriaga, M. P.; McBreen, J. *J. Electrochem. Soc.* **1995**, *142*, 1409−1422.

(13) Russell, A. E.; Tessier, B.; Wise, A.; Rose, A.; Price, S. W.; Richardson, P. W.; Ball, S.; Theobald, B.; Thompsett, D.; Crabb, E. M. *ECS Trans.* **2011**, *41*, 55−67.

(14) Jia, Q.; Liang, W.; Bates, M. K.; Mani, P.; Lee, W.; Mukerjee, S. *ACS Nano* **2015**, *9*, 387−400.

(15) Geiger, S.; Kasian, O.; Ledendecker, M.; Pizzutilo, E.; Mingers, A. M.; Fu, W. T.; Diaz-Morales, O.; Li, Z.; Oellers, T.; Fruchter, L.; Ludwig, A.; Mayrhofer, K. J. J.; Koper, M. T. M.; Cherevko, S. *Nat. Catal.* **2018**, *1*, 508−515.

(16) Jovanovič, P.; Hodnik, N.; Ruiz-Zepeda, F.; Arčon, I.; Jozinović, B.; Zorko, M.; Bele, M.; Šala, M.; Šelih, V. S.; Hočevar, S.; Gaberšček, M. *J. Am. Chem. Soc.* **2017**, *139*, 12837−12846.

(17) Jovanovič, P.; Pavlišič, A.; Šelih, V. S.; Šala, M.; Hodnik, N.; Bele, M.; Hočevar, S.; Gaberšček, M. *ChemCatChem* **2014**, *6*, 449−453.

(18) Hodnik, N.; Dehm, G.; Mayrhofer, K. J. J. *Acc. Chem. Res.* **2016**, *49*, 2015−2022.

(19) de Jonge, N.; Houben, L.; Dunin-Borkowski, R. E.; Ross, F. M. *Nat. Rev. Mater.* **2019**, *4*, 61−78.

(20) Wu, J.; Gao, W.; Yang, H.; Zuo, J.-M. *ACS Nano* **2017**, *11*, 1696−1703.

(21) Dai, S.; Hou, Y.; Onoue, M.; Zhang, S.; Gao, W.; Yan, X.; Graham, G. W.; Wu, R.; Pan, X. *Nano Lett.* **2017**, *17*, 4683−4688.

(22) Wang, C.; Chi, M.; Li, D.; Strmcnik, D.; van der Vliet, D.; Wang, G.; Komanicky, V.; Chang, K.-C.; Paulikas, A. P.; Tripkovic, D.; Pearson, J.; More, K. L.; Markovic, N. M.; Stamenkovic, V. R. *J. Am. Chem. Soc.* **2011**, *133*, 14396−14403.

(23) Cui, C.; Gan, L.; Heggen, M.; Rudi, S.; Strasser, P. *Nat. Mater.* **2013**, *12*, 765−771.

(24) Gan, L.; Cui, C.; Heggen, M.; Dionigi, F.; Rudi, S.; Strasser, P. *Science* **2014**, *346*, 1502−1506.

(25) Wang, D.; Yu, Y.; Zhu, J.; Liu, S.; Muller, D. A.; Abruña, H. D. *Nano Lett.* **2015**, *15*, 1343−1348.

(26) Mayrhofer, K. J. J.; Meier, J. C.; Ashton, S. J.; Wiberg, G. K. H.; Kraus, F.; Hanzlik, M.; Arenz, M. *Electrochem. Commun.* **2008**, *10*, 1144−1147.

(27) Meier, J. C.; Katsounaros, I.; Galeano, C.; Bongard, H. J.; Topalov, A. A.; Kostka, A.; Karschin, A.; Schüth, F.; Mayrhofer, K. J. *Energy Environ. Sci.* **2012**, *5*, 9319−9330.

(28) Hodnik, N.; Zorko, M.; Bele, M.; Hočevar, S.; Gaberšček, M. *J. Phys. Chem. C* **2012**, *116*, 21326−21333.

(29) Zorko, M.; Jozinović, B.; Bele, M.; Hodnik, N.; Gaberšček, M. *Ultramicroscopy* **2014**, *140*, 44−50.

(30) Jeyabharathi, C.; Hodnik, N.; Baldizzone, C.; Meier, J. C.; Heggen, M.; Phani, K. L. N.; Bele, M.; Zorko, M.; Hocevar, S.; Mayrhofer, K. J. J. *ChemCatChem* **2013**, *5*, 2627−2635.

(31) Jovanovič, P.; Ruiz-Zepeda, F.; Šala, M.; Hodnik, N. *J. Phys. Chem. C* **2018**, *122*, 10050−10058.

(32) Rasouli, S.; Myers, D.; Kariuki, N.; Higashida, K.; Nakashima, N.; Ferreira, P. *Nano Lett.* **2019**, *19*, 46−53.

(33) Heggen, M.; Gocyla, M.; Dunin-Borkowski, R. E. *Adv. Phys. X* **2017**, *2*, 281−301.

(34) Gatalo, M.; Jovanovič, P.; Polymeros, G.; Grote, J.-P.; Pavlišič, A.; Ruiz- Zepeda, F.; Šelih, V. S.; Šala, M.; Hočevar, S.; Bele, M.; Mayrhofer, K. J. J.; Hodnik, N.; Gaberšček, M. *ACS Catal.* **2016**, *6*, 1630−1634.

(35) Ruiz-Zepeda, F.; Gatalo, M.; Jovanovič, P.; Pavlišič, A.; Bele, M.; Hodnik, N.; Gaberšček, M. *ChemCatChem* **2017**, *9*, 3904−3911.

(36) Hodnik, N.; Jeyabharathi, C.; Meier, J. C.; Kostka, A.; Phani, K. L.; Rečnik, A.; Bele, M.; Hočevar, S.; Gaberšček, M.; Mayrhofer, K. J. *Phys. Chem. Chem. Phys.* **2014**, *16*, 13610−13615.

(37) Collings, E. W.; Enderby, J. E.; Ho, J. C. In Electronic density of states: Based on invited and contributed papers and discussion, Conference Proceedings ed.: 3rd Materials Research Symposium, Gaithersburg, MD, 1969; Bennett, L. H., Ed.; National Bureau of Standards: WA, 1971; pp 483−492.

(38) Bele, M.; Jovanovič, P.; Pavlišič, A.; Jozinović, B.; Zorko, M.; Rečnik, A.; Chernyshova, E.; Hočevar, S.; Hodnik, N.; Gaberšček, M. *Chem. Commun.* **2014**, *50*, 13124−13126.

(39) De Backer, A.; Martinez, G. T.; Mac Arthur, K. E.; Jones, L.; Béché, A.; Nellist, P. D.; Van Aert, S. *Ultramicroscopy* **2015**, *151*, 56−61.

(40) Van Aert, S.; De Backer, A.; Jones, L.; Martinez, G. T.; Béché, A.; Nellist, P. D. *Phys. Rev. Lett.* **2019**, *122*, No. 066101.

(41) McCue, I.; Snyder, J.; Li, X.; Chen, Q.; Sieradzki, K.; Erlebacher, J. *Phys. Rev. Lett.* **2012**, *108*, 225503.

(42) Egerton, R. F.; Li, P.; Malac, M. *Micron* **2004**, *35*, 399−409.

(43) Su, D. *Green Energy Environ.* **2017**, *2*, 70−83.

(44) Du, H. *Ultramicroscopy* **2015**, *151*, 62−67.

(45) Hodnik, N.; Zorko, M.; Bele, M.; Hočevar, S.; Gaberšček, M. *J. Phys. Chem. C* **2012**, *116*, 21326−21333.

(46) Oezaslan, M.; Heggen, M.; Strasser, P. *J. Am. Chem. Soc.* **2012**, *134*, 514−524.

(47) Altantzis, T.; Lobato, I.; De Backer, A.; Béché, A.; Zhang, Y.; Basak, S.; Porcu, M.; Xu, Q.; Sánchez-Iglesias, A.; Liz-Marzán, L. M.; Van Tendeloo, G.; Van Aert, S.; Bals, S. *Nano Lett.* **2019**, *19*, 477−481.

(48) De Backer, A.; van den Bos, K. H. W.; Van den Broek, W.; Sijbers, J.; Van Aert, S. *Ultramicroscopy* **2016**, *171*, 104−116.

(49) Pennycook, S. J.; Boatner, L. A. *Nature* **1988**, *336*, 565−567.

(50) Jones, L. *IOP Conf. Ser.: Mater. Sci. Eng.* **2016**, *109*, No. 012008.

(51) Stamenkovic, V. R.; Mun, B. S.; Mayrhofer, K. J. J.; Ross, P. N.; Markovic, N. M. *J. Am. Chem. Soc.* **2006**, *128*, 8813−8819.

(52) Pavlišič, A.; Jovanovič, P.; Šelih, V. S.; Šala, M.; Bele, M.; Dražić, G.; Arčon, I.; Hočevar, S.; Kokalj, A.; Hodnik, N.; Gaberšček, M. *ACS Catal.* **2016**, *6*, 5530−5534.

(53) Luo, M.; Guo, S. *Nat. Rev. Mater.* **2017**, *2*, 17059.

(54) De Backer, A.; van den Bos, K. H. W.; Van den Broek, W.; Sijbers, J.; Van Aert, S. *J. Phys.: Conf. Ser.* **2017**, *902*, No. 012013.

(55) De wael, A.; De Backer, A.; Jones, L.; Nellist, P. D.; Van Aert, S. *Ultramicroscopy* **2017**, *177*, 69−77.

(56) Galindo, P. L.; Kret, S.; Sanchez, A. M.; Laval, J. Y.; Yanez, A.; Pizarro, J.; Guerrero, E.; Ben, T.; Molina, S. I. *Ultramicroscopy* **2007**, *107*, 1186−1193.

(57) Pingel, T. N.; Jørgensen, M.; Yankovich, A. B.; Grönbeck, H.; Olsson, E. *Nat. Commun.* **2018**, *9*, 2722.

(58) Moseley, P.; Curtin, W. A. *Nano Lett.* **2015**, *15*, 4089−4095.

(59) Medasani, B.; Vasiliev, I. *Surf. Sci.* **2009**, *603*, 2042−2046.

(60) Tang, J.; Deng, L.; Xiao, S.; Deng, H.; Zhang, X.; Hu, W. *J. Phys. Chem. C* **2015**, *119*, 21515−21527.

(61) Vitos, L.; Ruban, A. V.; Skriver, H. L.; Kollár, J. *Surf. Sci.* **1998**, *411*, 186−202.

(62) Wen, Y.-Ni.; Zhang, J.-M. *Solid State Commun.* **2007**, *144*, 163−167.

(63) Peng, L.; Ringe, E.; Van Duyne, R. P.; Marks, L. D. *Phys. Chem. Chem. Phys.* **2015**, *17*, 27940−27951.

(64) Yun, K.; Cho, Y.-H.; Cha, P.-R.; Lee, J.; Nam, H.-S.; Oh, J. S.; Choi, J.-H.; Lee, S.-C. *Acta Mater.* **2012**, *60*, 4908−4916.

(65) Beermann, V.; Gocyla, M.; Willinger, E.; Rudi, S.; Heggen, M.; Dunin-Borkowski, R. E.; Willinger, M.-G.; Strasser, P. *Nano Lett.* **2016**, *16*, 1719−1725.

(66) Li, Y.; Hart, J. L.; Taheri, M. L.; Snyder, J. D. *ACS Catal.* **2017**, *7*, 7995−8005.

■ NOTE ADDED AFTER ASAP PUBLICATION

This paper was published ASAP on May 2, 2019 with an error in Figure 5. The corrected version was reposted on June 18, 2019.